A&A 607, A55 (2017)
DOI: 10.1051/0004-6361/201731392

Astronomy & Astrophysics

An 80 au cavity in the disk around HD 34282

G. van der Plas[1,2], F. Ménard[1], H. Canovas[3], H. Avenhaus[4,5], S. Casassus[2,5], C. Pinte[1], C. Caceres[6], and L. Cieza[5,7]

[1] Univ. Grenoble Alpes, CNRS, IPAG (UMR 5274), 38000 Grenoble, France
e-mail: info@gerritvanderplas.com
[2] Departamento de Astronomía, Universidad de Chile, Casilla 36-D, Santiago, Chile
[3] Departamento de Física Teórica, Universidad Autónoma de Madrid, Cantoblanco, 28049 Madrid, Spain
[4] ETH Zurich, Institute for Astronomy, Wolfgang-PauliStrasse 27, 8093 Zurich, Switzerland
[5] Millenium Nucleus Protoplanetary Disks in ALMA Early Science, Universidad de Chile, Casilla 36-D, Santiago, Chile
[6] Departamento de Ciencias Físicas, Facultad de Ciencias Exactas, Universidad Andrés Bello, Av. Fernàndez Concha 700, Las Condes, Santiago, Chile
[7] Nucleo de Astronomia, Facultad de Ingeniería, Universidad Diego Portales, Av. Ejércíto 441, Santiago, Chile

Received 18 June 2017 / Accepted 5 July 2017

ABSTRACT

Context. Large cavities in disks are important testing grounds for the mechanisms proposed to drive disk evolution and dispersion, such as dynamical clearing by planets and photoevaporation.
Aims. We aim to resolve the large cavity in the disk around HD 34282, whose presence has been predicted by previous studies modeling the spectral energy distribution of the disk.
Methods. Using ALMA band 7 observations we studied HD 34282 with a spatial resolution of $0.10'' \times 0.17''$ at 345 GHz.
Results. We resolve the disk around HD 34282 into a ring between 0.24″ and 1.15″ (78^{+7}_{-11} and 374^{+33}_{-54} au adopting a distance of 325^{+29}_{-47} pc). The emission in this ring shows azimuthal asymmetry centered at a radial distance of 0.46″ and a position angle of 135° and an azimuthal FWHM of 51°. We detect CO emission both inside the disk cavity and as far out as 2.7 times the radial extent of the dust emission.
Conclusions. Both the large disk cavity and the azimuthal structure in the disk around HD 34282 can be explained by the presence of a 50 $M_{\rm jup}$ brown dwarf companion at a separation of ≈0.1″.

Key words. stars: variables: T Tauri, Herbig Ae/Be – protoplanetary disks

1. Introduction

Protoplanetary disks are the birth environments of planetary systems. How these planets form is an ongoing topic of debate that is informed by an increasing number of disks that show various degrees of evolution and dispersal, such as opacity cavities (transitional disks), gaps (pre-transitional disks, e.g. Williams & Cieza 2011), and asymmetrical (lopsided) emission features. Examples of such disks imaged at (sub) mm wavelengths include HD 100546 (Walsh et al. 2014), Sz 91 (Canovas et al. 2015, 2016), HD 142527 (Casassus et al. 2013), HD 97048 (van der Plas et al. 2017) and SAO 206462 (Brown et al. 2009).

The common denominator between these disks is that their structure can be described by one large cavity or a broad ring of dust grains at reasonably large radii combined with multiple rings, gaps and/or azimuthal horseshoe-shaped asymmetries in the outer disk. The gaps and/or cavities in these disks are not empty: they contain both smaller dust grains, as traced by scattered light imaging (e.g., Kraus & Ireland 2012; Avenhaus et al. 2014), and gas, as most readily traced by rotational (Perez et al. 2015a; van der Marel et al. 2015) and rovibrational carbon monoxide (CO) lines (van der Plas et al. 2009, 2015; Pontoppidan et al. 2011; Carmona et al. 2014). Recently, long baseline Atacama Large Millimeter Array (ALMA) observations of HL Tau (ALMA Partnership et al. 2015), HD 163296 (Isella et al. 2016), and TW Hya (Andrews et al. 2016; Nomura et al. 2016; Tsukagoshi et al. 2016) have demonstrated that these disks show a rich substructure of many concentric rings and gaps at scales as small as 1 au when observed at very high spatial resolution. It is indeed possible that most disks contain similar detailed structures that have not yet been resolved (Zhang et al. 2016).

Radial and azimuthal asymmetries in the dust emission structure of disks reflects variations in either the underlying mass, grain properties (size distribution), and/or temperature. The response of the disk to local pressure maxima is a frequently invoked mechanism to explain these structures. A local maximum in the gas density preferentially traps larger grains and thus stops the inward drift motion caused by the aerodynamic drag of the gas on the dust (Weidenschilling 1977), allowing dust grains to accumulate in these so-called dust traps. Such local gas pressure maxima have many proposed origins; for example, the maxima are generated at the edge of a dead zone (Dzyurkevich et al. 2010), by MRI instabilities (Uribe et al. 2011), or at the edge of a planet-carved gap (e.g. Pinilla et al. 2012). These maxima can even form spontaneously in simulations when the growth and fragmentation of dust grains and the back reaction of the dust grains on the gas is taken into account (Gonzalez et al. 2017). Jumps in the pressure gradient can also induce vortices due to Rossby wave instability (RWI, e.g. Lovelace et al. 1999; Lyra & Lin 2013). Such vortices are especially promising places

Table 1. Details of the observations.

UT date	Number antennas	Baseline range (m)	*pwv* (mm)	Flux	Calibrators: Bandpass	Gain
2014 Dec. 12	37	15.1 to 348.5	0.811	J0423-013	J0522-3627	J0501-0159
2015 Aug. 31	38	15.1 to 1466.2	0.755	J0423-013	J0423-0120	J0542-0913

for planetesimal formation given their high efficiency in concentrating large dust masses (Meheut et al. 2012). A RWI however is only stable in low viscosity disks with $\alpha \lesssim 10^{-4}$ (de Val-Borro et al. 2007). Another mechanism proposed to explain horseshoe-shaped features in disks is the presence of an unequal-mass binary companion. For large enough mass ratios the cavity becomes eccentric causing an azimuthally localized gas overdensity on the outer edge of the cavity (Ragusa et al. 2017).

Detection and characterization of more structured disks are necessary to determine the physical origin of these asymmetries. Disks around the intermediate mass Herbig Ae/Be (HAeBe) stars are good candidates for spatially resolving such structures, given their higher brightness and larger size compared to disks around the more abundant but lower mass/luminosity T Tauri stars. These disks have historically been split into two groups based on the shape of their spectral energy distribution (SED). Group I sources display relatively bright mid- to far-infrared emission and have been interpreted as hosting gas-rich protoplanetary disks with a flared, bright dust surface. Most dust in group II disks is assumed to have settled toward the midplane and these disks therefore emit weaker mid- to far-infrared emission (Meeus et al. 2001; Dullemond & Dominik 2004). Recent modeling of resolved observations of group I sources suggests that the bright infrared emission of these sources should instead be attributed to the large vertical walls on the limit of (large) dust cavities (Honda et al. 2012; Maaskant et al. 2013); this idea is supported by high resolution scattered light imaging (Garufi et al. 2017) and spatially resolved CO rovibrational observations (van der Plas et al. 2015).

In this manuscript we present ALMA observations of the group I disk around the Herbig Ae/Be star HD 34282. The disk around this star has already been resolved using 1.3 mm continuum emission with a FWHM of $1.74'' \times 0.89''$ (Piétu et al. 2003) and with rotational CO lines (Greaves et al. 2000; Piétu et al. 2003). Acke et al. (2009) predicted the presence of an opacity cavity in this disk based on modeling the SED. Khalafinejad et al. (2016) used spatially resolved Q-band emission to estimate a gap that is 92 (+31, −17) au in size.

Multiple estimates of the stellar parameters for HD 34282 exist. We use the values derived by Merín et al. (2004) that are based on detailed modeling of the stellar spectrum and the SED. These authors found low metal abundances in the stellar spectrum and derived an A3 V spectral type, an age of $6.4^{+1.9}_{-2.6}$ Myr, a luminosity of $13.64^{+5.36}_{-12.02}$ $L_\odot$, and a mass of $1.59^{+0.30}_{-0.07}$ $M_\odot$ for the central star. For the source distance we use the value of 325^{+29}_{-47} pc from the *Gaia* DR1 (Gaia Collaboration 2016a,b). This value is within the 1σ values on the distance determined by Merín et al. (2004) of 348^{+129}_{-77} and of 400^{+170}_{-100} pc (Piétu et al. 2003).

2. Observations and data reduction

ALMA Early Science Cycle 2 observations were conducted in the compact C43-2 configuration on December 12, 2014 with 684 s of total time on source and in an extended C34-7 configuration on August 31, 2015 with 342 s of total time on source. The array configuration provided baselines ranging between 15.1 and 348.5 m and between 15.1 and 1466.2 m, respectively. During the observations the precipitable water vapor had a median value at zenith of 0.811 and 0.755 mm, respectively.

Two of the four spectral windows of the ALMA correlator were configured in time division mode (TDM) to maximize the sensitivity for continuum observations (128 channels over 1.875 GHz usable bandwidth). These two TDM spectral windows were centered at 345.8 and 356.7 GHz. The other two spectral windows were configured in frequency division mode (FDM) to target the ^{12}CO $J = 3{-}2$ and the HCO$^+$ $J = 4{-}3$ lines with a spectral resolution of 105 and 103 m s^{-1}, respectively, using 0.23 GHz total bandwidth. The data were calibrated and combined using the *Common Astronomy Software Applications* pipeline (CASA, McMullin et al. 2007, version 4.5). Inspection of the calibrated visibilities shows a 20% difference in amplitude between the two observations at short baselines. Given that the estimated error on the flux calibrator for the extended array configuration observations is twice as large as that for the compact configuration observations and assuming that the emission from the midplane is constant in the eight month period spanning the observations, we scaled the amplitudes of the visibilities for the extended array configuration observations to those of the compact array configuration observations. Details of the observations and calibration are summarized in Table 1, we estimated the absolute flux calibration to be accurate within ∼20%.

We imaged the disks with the CLEAN task in CASA (Högbom 1974) using Briggs and superuniform weighting, which results in a restored beam of $0.25'' \times 0.19''$ at PA = 88.3° (Briggs) and $0.17'' \times 0.10''$ at PA = 77.0° (superuniform), respectively. The dynamic range of these images is strongly limited by the bright continuum source and we performed self-calibration on both phase and amplitude, resulting in a final rms of 0.11 mJy/beam for the images created using superuniform weighting. We show the resulting continuum map in Fig. 1. We applied the self-calibration solutions obtained from the continuum emission to the HCO$^+$ and CO calibrated visibilities and subtracted the continuum emission using the CASA task *uvcontsub*. The resulting integrated intensity (moment 0), intensity-weighted mean velocity (moment 1) and peak intensity (moment 8) maps and spectra are shown in Figs. 2 and 3 for the CO $J = 3{-}2$ and HCO$^+$ $J = 4{-}3$ emission, respectively.

3. Results

3.1. Continuum

The HD 34282 dust continuum emission is concentrated into a ring that shows an azimuthal variation in intensity (Fig. 1). We use the fitting library *uvmultifit* (Martí-Vidal et al. 2014) to fit a superposition of simple geometrical shapes to the continuum visibilities to estimate the inclination, position angle, and spatial distribution of the emission. The *uvmultifit* fitting library minimizes χ^2 as a function of the input model parameters. Quoted

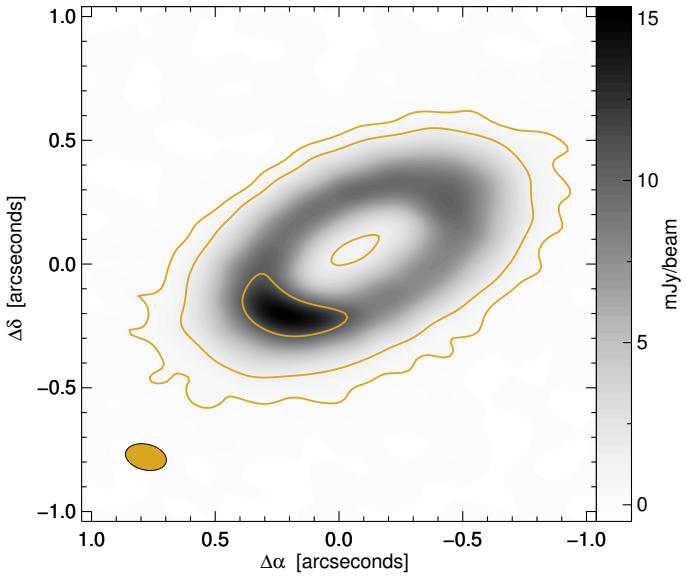

Fig. 1. Continuum image of HD 34282 for the ALMA band 7 (351.24 GHz or 0.853 mm) observations, reconstructed using superuniform weighting resulting in a 0.10″ × 0.17″ beam. Overplotted are contours at 5, 15 and 100 times the rms value of 0.11 mJy/beam. The beam is shown in orange in the bottom left.

parameter uncertainties are estimated from the post-fit covariance matrix which is scaled so that its χ^2_r has a value of 1.

We fit the continuum visibilities to a combination of the following geometries: (1) a disk with a constant surface brightness; (2) an unresolved ring; and (3) a 2D Gaussian whose size and center are left free. Each of these elements has the following free parameters: offset in RA and Dec from the phase center, flux, semimajor axis, axis ratio, and position angle. The disk element has two values for the semimajor axis: one for the inner radius of the disk (the cavity radius) and one for the outer radius of the disk. When fitting two disks or a disk and a ring simultaneously we force them to share the same center, inclination, and position angle. We fit these shapes for each of the continuum windows (at 345.8 and 356.7 GHz) separately to allow the detection of possible changes in flux due to the spectral slope of the dust emission α ($S_\nu \propto \nu^\alpha$).

We achieve the best fit with a combination of two disk components and a Gaussian that is offset from the disk center, as judged by minimizing the residuals of the calibrated visibilities of the data and our models. The best-fit parameters for the fitted components are listed in Table 2 and are visualized in Fig. 4, in which we compare the imaged model and residuals to the HD 34282 disk, together with the real part of the visibilities for the data, the model, and their differences. Overall, our best fit provides a reasonable match to the data. The center of the cavity is in agreement with the stellar position published in the *Gaia* DR1 (Gaia Collaboration 2016a,b), and the dominant source of residuals is a radial pattern alternating between negative and positive signals that are most visible along the major axis of the disk. This pattern is a consequence of using disk models with a radial constant surface brightness and a sharp drop at the disk boundary. The most significant non-radially symmetric residuals are visible at the far side of the disk close to the disk minor axis, on the order of 1.0 mJy/beam, nine times the image rms.

We start our analysis with the following values derived from our best fit: a disk with a total flux of 323.9 mJy at 345.8 GHz (867 μm) with a spectral slope of -3.0 ± 0.7 coming from a disk that extends between 0.24″ and 0.94″, an inclination of 59.3° and a position angle of 117.1°.

3.1.1. Radial and azimuthal structure of the dust emission

From fitting the visibilities with a superposition of simple geometrical shapes we find that ≈95% of the continuum emission originates from a ring between 0.24 and 0.94″ from the central star, while the remaining 5% are concentrated in a region that is elongated in the azimuthal direction at a radial distance of ≈0.36″ from the star atop the smooth disk. Looking at the imaged residuals (Fig. 4) there are hints of faint emission both inside the cavity and outside the fitted rings.

The emission within the cavity, also visible in the imaged residuals, indicates that there is at least some dust inside the fitted cavity radius at 0.24″. The amplitude of this residual emission is comparable to that of the residuals at the inner and outer boundaries of the fitted disks, and is likely caused by our choice of fitting a disk with a sharp edge.

To better characterize the radial and azimuthal structure of the dust disk, we remapped the disk to polar coordinates after deprojecting it using the previously derived geometry (Fig. 5). The intensity profile in polar coordinates is shown in the top left panel and is collapsed in the radial (top right panel) and azimuthal (bottom left panel) dimensions to obtain the respective integrated surface brightness structures.

The radial brightness profile for the continuum emission rises monotonically until it peaks at 0.44″. After that it decreases and shows a change in slope around 1.15″ until it becomes indistinguishable from the background around 1.35″, as shown in the bottom left panel of Fig. 5. The radial brightness distribution of the dust continuum emission between the peak at 0.44″ and the outer disk radius at 1.35″ can be fitted by two power laws separated at 1.15″ with exponents of −6 and −16, respectively.

The azimuthal brightness profile for the continuum emission peaks at an azimuth of 135° with a maximum ≈25% above the median value for the disk and 18° away from the major axis of the disk. To further study the azimuthal structure of the disk we subtract a median *radial* Gaussian profile from each azimuthal row in the polar projection. We create this average Gaussian by selecting only those radial slices with an integrated value within 1% of the median integrated value over all azimuths (Fig. 6). The remaining structure peaks close to the major axis of the disk and is best fit with a 2D Gaussian centered on (radius, azimuth) =(0.43″, 18°) with a FWHM of 0.15″ in radius and 52° in azimuth. This feature is discussed in Sect. 4.

3.2. CO and HCO^+ emission

We detect spatially and spectrally resolved emission from the ^{12}CO $J = 3{-}2$ and HCO^+ $J = 4{-}3$ emission lines from the HD 34282 disk. We show the moment maps and line profiles in Figs. 2 and 3 respectively.

We estimate the systemic velocity from the ^{12}CO $J = 3{-}2$ emission line at $v_{\rm LSR} = -2.35 \pm 0.10$ km s^{-1}, based on the center of the line profile and channel maps. The line flux, integrated between + and −6.75 km s^{-1} from the systemic velocity is 21.2 ± 0.3 Jy km s^{-1}. The semimajor axis, as measured from the ^{12}CO moment maps is 3.1″. We detect ^{12}CO emission coming from within the disk cavity and see two layers of CO emission on either side of the disk surface (Fig. 7), which shows that the ^{12}CO emission originates from the warm disk surface on both

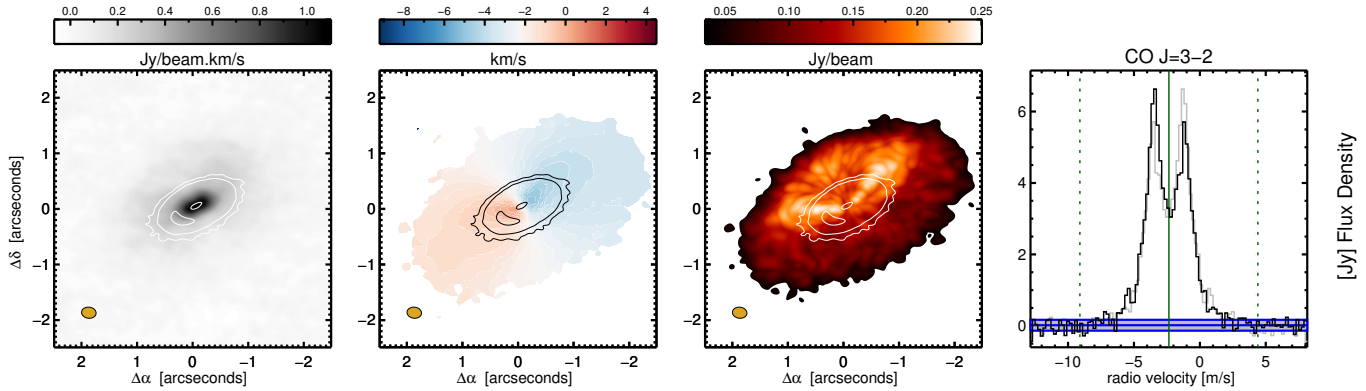

Fig. 2. Summary of ^{12}CO $J = 3–2$ line emission from the disk around HD 34282. We show the integrated intensity (moment 0, *left panel*), intensity-weighted velocity (moment 1, 2*nd panel*), peak intensity (moment 8, 3*rd panel*) and the collapsed emission line (*right panel*). Each moment map was made using a 5σ cutoff and imaged using Briggs weighting. Overplotted in the *three left panels* are continuum contours with [5, 15 and 100] times the rms value of the continuum map imaged using superuniform weighting. The beam is shown in orange in the bottom left of each panel. The grayshaded area in the *right panel* denotes the + and –3σ level calculated outside the line boundaries.

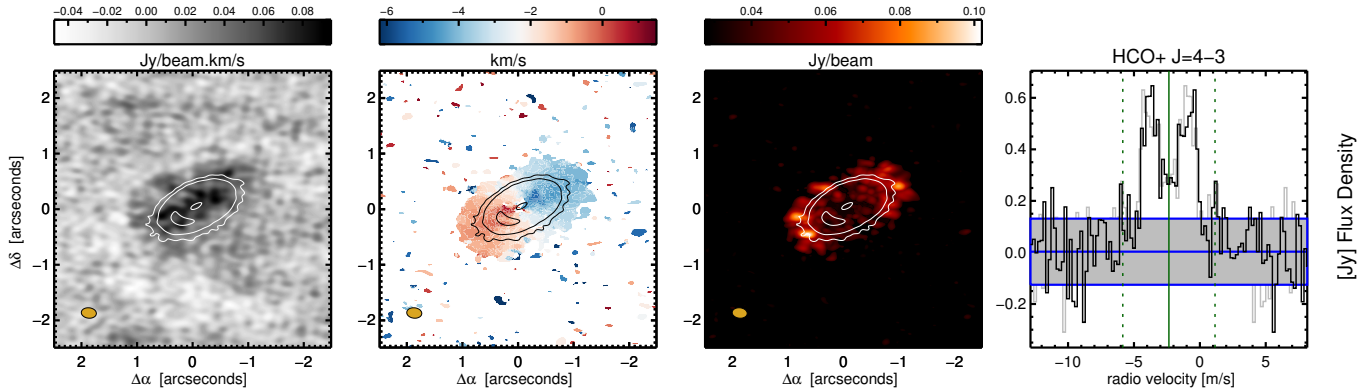

Fig. 3. Summary of HCO$^+$ $J = 4–3$ line emission in HD 34282. We show the integrated intensity (moment 0, *left panel*), intensity-weighted velocity (moment 1, 2*nd panel*), peak intensity (moment 8, 3*rd panel*) and the collapsed emission line (*right panel*). Each moment map was made using a 3σ cutoff and imaged using Briggs weighting. Overplotted in the *three left panels* are continuum contours with [5, 15 and 100] times the rms value of the continuum emission. The beam is shown in orange in the *bottom left of each panel*. The grayshaded area in the *right panel* denotes the + and –3σ level calculated outside the line boundaries.

faces of the disk. We calculate an upper limit on the inner radius of the gas disk assuming Keplerian rotation for the highest velocity at which we detect the line above 3σ, and measure the radial outer extent of the gas disk based on the presence of emission above three times the rms value. We summarize the measured gas disk size and line flux in Table 3. In the naturally weighted channel maps CO emission >3σ is present between −8.8 and +4.6 km s^{-1}. These values can be translated to an emitting radius of ≈23 au, assuming the gas is in Keplerian rotation in a disk inclined by 59.3° around a 1.59 $M_\odot$ star.

The low-J ^{12}CO rotational emission lines in protoplanetary disks become optically thick quickly and trace a vertically thin region in the line of sight up to where the line becomes optically thick, making them a tracer of disk geometry (e.g. de Gregorio-Monsalvo et al. 2013; Woitke et al. 2016). This makes it possible to infer the disk geometry and spatial extend from the ^{12}CO $J = 3–2$ moment 8 (peak intensity) map shown in Fig. 2, panel 3. Warmer CO gas emits stronger per unit volume, and the modulation of the peak brightness over the disk surface can be naturally interpreted as looking into a flared disk (bowl) where the far side of the disk is the warm and directly irradiated disk surface. This warm surface is shielded by the flaring outer disk on the near (south-west) side, from which we instead see the cooler midplane and the backside of the disk.

The HCO$^+$ emission is less extended with a semimajor axis of 1.3″ and is, with a flux of 2.2 ± 0.2 Jy km s^{-1}, 10 times weaker than the CO emission. Based on the resolved emission in the channel maps the emission comes from deeper in the disk (closer to the midplane) and emission >3σ is present between −5.8 and +1.2 km s^{-1}. These values can be translated to an emitting inner radius of ≈85 au, assuming the gas is in Keplerian rotation in a disk inclined by 59.3° around a 1.59 $M_\odot$ star. The HCO$^+$ is brightest beyond the outer radius of the continuum ring, as seen in the moment 8 map in Fig. 3. We confirm that this is an artifact of subtracting the continuum from the HCO$^+$ emission by repeating our analysis using the non-continuum-subtracted data. This suggests either that the continuum is absorbing part of the line emission mostly from the far side of the disk or that the HCO$^+$ emission is optically thick.

4. Discussion

In the following section we discuss the mass of the disk and its components, the spatial distribution of the dust and gas, and possible mechanisms that can provoke such a system architecture.

Table 2. Best-fit parameters with their respective 1σ uncertainty in parenthesis, obtained from fitting separate components to the continuum visibilities: either one component (radially constant disk, a ring, and a Gaussian) or a combination of these components.

Component	ΔRA[a] ["]	ΔDec[a] ["]	$S_{\nu,345.8\ \mathrm{GHz}}$ [mJy]	α	Semimajor axis ["]	Inclination [°]	PA [°]	X^2_r
1 component								
Gaussian (G)	–0.039	0.017	338.0 (0.7)	–3.2 (0.1)	0.53 (0.01)	60.4 (0.4)	119.4 (0.4)	9.69
Ring (R)	–0.046	0.022	312.3 (0.5)	–2.9 (0.1)	0.50 (0.01)	59.0 (0.3)	116.7 (0.4)	9.30
Disk (D)	–0.044	0.021	322.4 (0.6)	–3.1 (0.1)	0.19 (0.07), 0.74 (0.03)[b]	59.4 (0.6)	117.5 (0.4)	8.97
>1 components								
D + R								
Disk 1	–0.053	0.029	252.6 (1.3)	–3.2 (0.2)	0.21 (0.02), 0.75 (0.01)[b]	59.7 (0.4)	118.0 (0.1)	
Ring 1	fixed	fixed	65.6 (1.3)	–1.6 (0.9)	0.45 (0.01)	fixed	fixed	
Total			318.2 (1.8)	–2.9 (0.4)				5.76
D + D								
Disk 1	–0.053	0.029	215.1 (2.1)	–3.1 (0.5)	0.26 (0.02), 0.61 (0.01)[b]	59.6 (0.4)	117.9 (0.3)	
Disk 2	fixed	fixed	108.1 (2.2)	–2.8 (1.0)	0.32 (0.06), 0.90 (0.01)	fixed	fixed	
Total			323.1 (3.0)	–3.0 (0.6)				5.50
D + D + G								
Disk 1	–0.063	0.039	221.2 (2.1)	–4.5 (1.1)	0.24 (0.01), 0.63 (0.01)[b]	59.3 (0.4)	117.1 (0.3)	
Disk 2	fixed	fixed	87.0 (2.1)	–2.5 (0.5)	0.34 (0.07), 0.94 (0.01)	fixed	fixed	
Gaussian	0.270[c]	–0.240[c]	15.7 (0.3)	–1.5 (1.1)	0.15 (0.01)	70.1 (1.0)	67.4 (4.6)	
Total			323.9 (3.0)	–3.0 (0.7)				5.41

Notes. When fitting a disk and ring component simultaneously, the following parameters were fixed between the two: the offset from the pointing center, the inclination, and position angle. In the table we represent these values as "fixed". The spectral slope α (5th column) is calculated following $S_\nu \propto \nu^\alpha$. [(a)] Offset from the pointing center. [(b)] Contains two values for the disk component: the inner and outer radius. [(c)] Offset relative to the center of the best-fit disk and ring component.

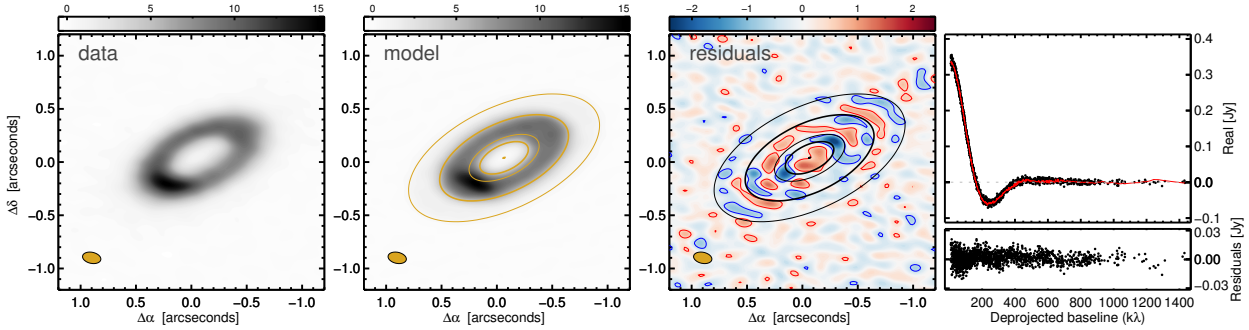

Fig. 4. Comparison of ALMA band 7 data (*left panel*) with the best-fit composite "disk + disk + Gaussian" model (*2nd panel*). The *3rd panel* shows the imaged residuals. We draw red and blue contours at 5 times the image rms of 0.11 mJy. Units of all intensity scales are in mJy/beam. The central two panels include ellipses representing the 2 fitted disk components to guide the eye. These are drawn at the radial location corresponding to the inner and outer disk radius for disk #1 (thick line) and disk #2 (thin line), as summarized in Table 2. The *right panel* (*top*) shows the real part of the visibilities as function of the deprojected baseline for the data (black dots) and the model (red line). The *bottom panel* shows the residuals. The visibilities are binned in sets of 200.

4.1. Mass limits on the disk and vortex-shaped feature

A coarse but straightforward way to relate observed sub-mm fluxes to dust mass is by assuming the emitting dust is optically thin and of a single (average) temperature,

$$\log M_{\mathrm{dust}} = \log S_\nu + 2\log d - \log \kappa_\nu - \log B_\nu(\langle T_{\mathrm{dust}}\rangle), \quad (1)$$

where S_ν is the flux density, d is the distance, κ_ν is the dust opacity, and $B_\nu(\langle T_{\mathrm{dust}}\rangle)$ is the Planck function evaluated at the average dust temperature (Hildebrand 1983). We adopt a dust opacity of 2.7 cm^2 g^{-1} at 0.867 mm, calculated using smoothed UV astronomical silicate (Draine & Lee 1984; Laor & Draine 1993; Weingartner & Draine 2000) with a grain size distribution with sizes between 0.1 and 3000 μm distributed following a power law with a slope of −3.5. We estimate the average dust temperature using the correlation with stellar luminosity $\langle T_{\mathrm{dust}}\rangle \approx 25(L_*/L_\odot)^{1/4}$ K (e.g. Andrews et al. 2013), leading to a $\langle T_{\mathrm{dust}}\rangle$ of 48 K. This is most likely an overestimate of the dust temperature since all dust in the disk around HD 34282 is located outside ≈78 au and the resulting dust mass should thus be interpreted as a lower limit. Using these assumptions, we calculate a dust mass of 0.41 M_{jup} for the disk and 6.6 M_{earth} for the vortex-shaped feature. With a dust-to-gas ratio of 1:100 this leads to a disk that weights 2.5% of the stellar mass. The line-of-sight optical depth, which i calculated with the parameters of our best-fit disk model, a dust opacity of 2.7 cm^2 g^{-1}, and an albedo of 0.75, is 1.1 in the vortex-shaped feature and 0.6 along the ring.

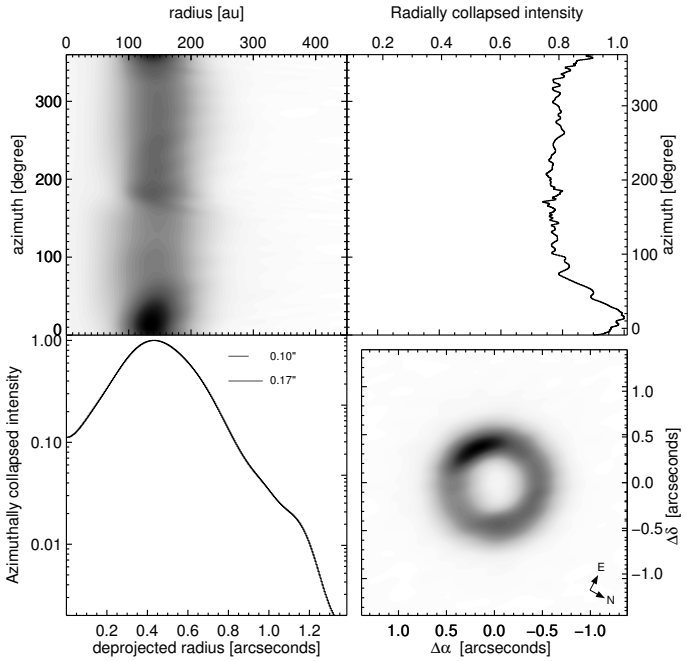

Fig. 5. ALMA band 7 image reconstructed using superuniform weighting, deprojected using the disk inclination and rotated with the position angle listed in Table 2 to put the major axis of the disk at 0° (north; *bottom right panel*), converted to polar coordinates (*top left panel*). This polar map is collapsed along the radial and azimuthal axes to yield the azimuthal intensity distribution (*top right*) and the radial intensity distribution (*bottom left*). In this *last panel* we also show the size of the beam minor and major axis for reference.

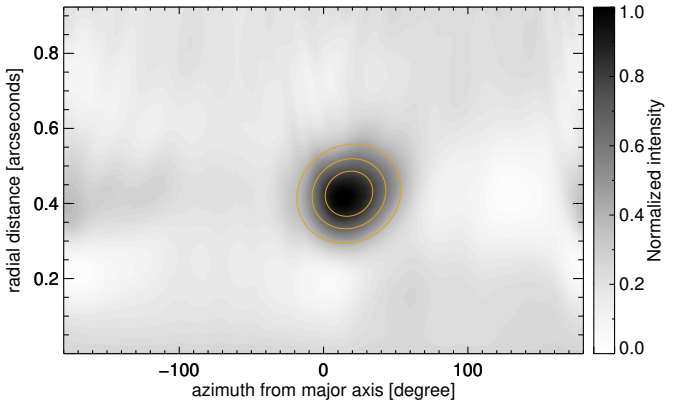

Fig. 6. Surface brightness of the disk after subtracting a Gaussian fit to the median radial profile, shown in polar coordinates with the position angle relative to the major axis of the disk on the x-axis and the radial distance from the center on the y-axis. Contours of the best-fit 2D Gaussian are show at values of [0.25, 0.5 and 0.75] times its peak value.

4.2. Radial and azimuthal structure of the dust emission

Both defining features of the dust continuum emission, the ring and the azimuthal asymmetry, can be explained by the dynamics of gas and dust at the edge of the cavity if there is an unseen massive companion present. Ragusa et al. (2017) use 3D SPH gas and dust simulations to test the effect of a binary pair of unequal mass on a circumbinary disk. In their simulations the companion carves a wide and eccentric cavity resulting in a non-axisymmetric gas overdensity at the cavity edge. The amount of azimuthal asymmetry in their simulations scales with the binary mass ratio; a ratio of 0.01 results in a ring-like structure, while a mass ratio of 0.05 produces a contrast ratio of ≈1.5 between the feature and background disk. Since the brightness contrast ratio in the HD 34282 disk is ≈1.25, a naive interpolation would put the companion mass at ≈0.05 $M_\odot$ (50 $M_{\rm jup}$).

The presence of a binary companion has already been suggested by Wheelwright et al. (2010) based on the spectro-astrometric signal of the Hβ line. No estimate of the separation or position angle is given, however, owing to artifacts in the astrometric signal. The spectro-astrometric technique used is sensitive to binaries with a separation between 0.1″ and 2″ with a brightness contrast of up to 5 mag (Baines et al. 2006), putting the companion somewhere between 0.1″ and the cavity radius at 0.24″. A separation close to 0.1″ is in agreement with predictions by Artymowicz & Lubow (1994) for the location of the cavity outer edge, who predict the inner edge for the circumbinary disk to be between 1.8 to 2.6 times the binary semimajor axis for low (between 0 and 0.25) eccentricities.

This scenario, where a brown dwarf binary companion induces the outer disk morphology, is backed up by the following arguments:

(1) Besides dynamical clearing, inside-out photoevaporation of the disk by the stellar radiation is often invoked as cause for disk cavities (e.g. Clarke et al. 2001; Alexander et al. 2006; Owen et al. 2010). However, in the case of this disk we deem photoevaporation unlikely to have shaped the cavity. The nondetection of CO gas close to the star in both the rotational (this work) and rovibrational lines (Carmona et al. 2005) is consistent with a photoevaporation scenario. However, an important caveat is the sensitivity of the latter CO observations. Typical line strengths for CO rovibrational lines originating from disks around HAeBe disks are about 5 to 10% above the continuum level (e.g. van der Plas et al. 2015). Such lines could easily be hidden in the noise given the spectrum presented in Fig. 1 of Carmona et al. (2005), which makes HD 34282 a prime target for high sensitivity observations of the fundamental rovibrational CO lines.
The arguments against photoevaporation as a cause for the cavity are stronger. Cavities carved out by radiation pressure from the central star are predicted to have a sharp edge, which is not the case for the HD 34282 disk. The inside-out nature of photoevaporation as a root cause for the cavity also precludes the presence of any inner disk, while a halo or small inner disk is required to fit the near-infrared (NIR) excess observed for this source (Khalafinejad et al. 2016).
(2) The stellar Fe/H abundance for HD 34282 is strongly depleted; this is in line with the suggestion by Kama et al. (2015) that depletion of heavy elements emerges as companions block the accretion of part of the dust, while gas continues to flow toward the central star.

The spectral index value we derive for the complete disk (-3.0 ± 0.7) is lower than, but within uncertainty consistent with, the canonical value of ≈–2.3 for disks (Testi et al. 2014). This lower value is in line with the trend observed in, for example, AS 209, where the grain size distribution is weighted more toward larger grains in the inner disk leading to a value of $\alpha > -2.5$ at 20 au and increasing to <–3.5 outside 80 au (Pérez et al. 2012).

One out of the three components, the Gaussian offset from the disk center, in our best-fit disk model deviates >1σ from the typical value for young disks of −2.3, whereas the small value of α in the fitted Gaussian suggests advanced grain growth. However, given the large error on this value we do not consider this deviation significant. Upcoming work on this source, comparing these data with 1.3 mm ALMA measurements at a similar

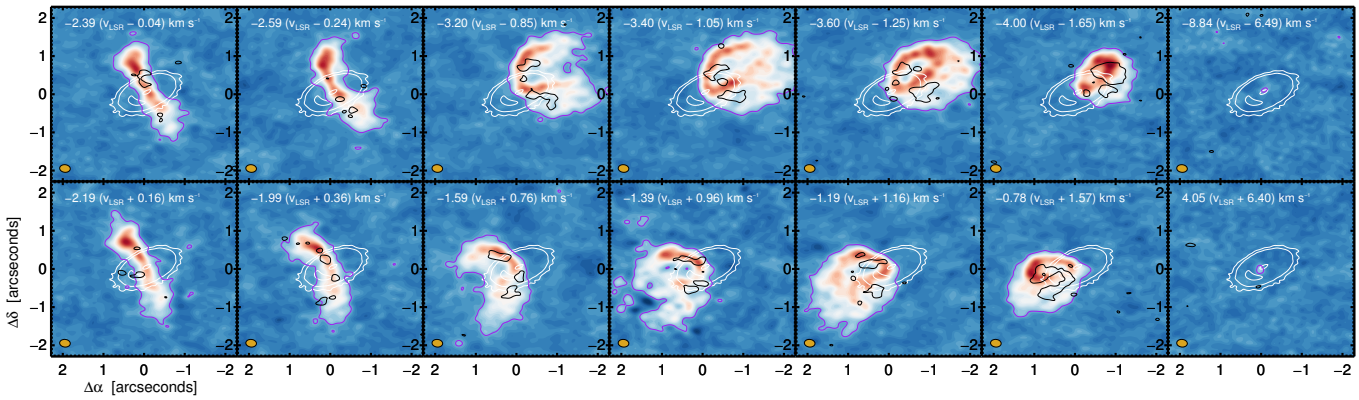

Fig. 7. Selected channel maps showing the CO channels in color and their 3σ outline in purple, the HCO^+ emission 3σ outline with black contours, and the continuum contours in white. In the *top right* of each panel the v_{lsr} is indicated in white noting the velocity with respect to the systemic velocity of -2.35 km s^{-1} in parenthesis. The clean beam is shown in yellow in the bottom left of each panel.

Table 3. Line fluxes, spectral resolution and spatial extent for the CO $J = 3-2$ and HCO^+ $J = 4-3$ lines.

Line	Line flux (Jy km s^{-1})	Error[a] (Jy km s^{-1})	Channel width (m s^{-1})	rms[b] (mJy/beam)	Major axis[c] ″	r_{in}[d] (au)
CO $J = 3-2$	21.2	0.3	200	9.4	6.2	23
HCO^+ $J = 4-3$	2.2	0.2	200	10.4	2.6	85

Notes. Line fluxes have been calculated from the Briggs-weighted images by integrating the emission around the systemic velocity at -2.35 km s^{-1} assuming a half line width of 3.5 km s^{-1} for the HCO^+ $J = 4-3$ line and 6.75 km s^{-1} for the CO $J = 3-2$ line. [(a)] Estimated from the rms of the integrated spectrum outside the line boundaries, does not include calibration uncertainties. [(b)] 1σ rms per channel. [(c)] Major axis is determined for all emission above 3 times the rms per channel. [(d)] Calculated from the maximum velocity for which emission $>3\sigma$ is present in the channel maps, assuming the gas is in Keplerian rotation in a disk inclined with 59.3° around a 1.59 $M_\odot$ star.

angular resolution, will be better able to decide the nature of the azimuthal brightness modulation. This azimuthally asymmetric feature in the disk originates from the same radial distance as the peak emission of the dust ring as can be seen in Fig. 6. The radial size of the disk is comparable to the beam and thus could be unresolved. The feature is resolved in the azimuthal direction with a FWHM of 52°.

4.3. Distribution and kinematics of the gas

It is possible that CO gas is present closer to the star than the 24 au limit measured from our data because beam dilution would render the emission undetectable given the size of our beam (65×85 au for the Briggs-weighted maps). In the outer disk regions the CO gas can be traced out as far as 3.1″ (1000 au), which is a factor of ≈2.7 further out than the dust detection coming from larger grains.

Judging by the velocity field, the CO emission is in agreement with that from a Keplerian rotating disk. We verify our choice for distance (325 au) and stellar mass (1.59 $M_\odot$) using kinematics of the CO emission. We construct a position-velocity map using the disk position derived from fitting the continuum emission and compare this with the expected Keplerian rotation curves for the stellar distance and mass derived by Piétu et al. (2003) and Merín et al. (2004), respectively, in Fig. 8. The inner radius for the CO rotation curves is set at 24 au and the outer radius is set either at 835 au (from Piétu et al. 2003) or at 1080 au.

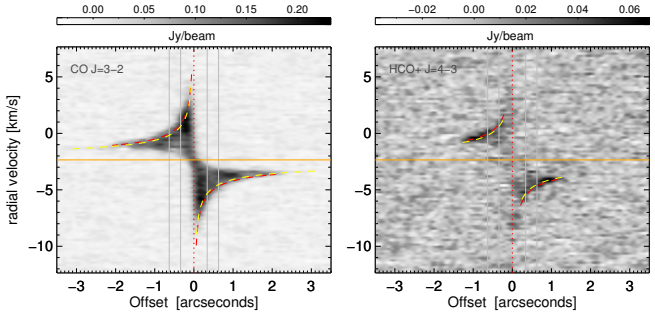

Fig. 8. Position-velocity diagram for the CO $J = 3-2$ (*left*) and HCO^+ $J = 3-2$ (*right*) emission made using the disk center and position angle listed in Table 2. We use a dotted vertical red line to show the stellar position. The systemic velocity of -2.35 km s^{-1} is shown with an orange horizontal line. We show the Keplerian rotation curves for the two different estimates for stellar mass and distance from Merín et al. (2004; yellow: $M_* = 1.59$ $M_\odot$ and $d = 348$ pc) and from Piétu et al. (2003; red: $M_* = 2.1$ $M_\odot$ and $d = 400$ pc). The radial inner and outer extent of the curves is taken from the inner and outer radius of the emission listed in Table 3. We also overplot in both panels with gray vertical lines the radial distances of 0.34″ and 0.63″ to mark the band where the continuum emission is strongest.

The CO outer disk size derived in this work scaled to the stellar distance of Merín et al. (2004). For the HCO^+ PV diagrams we draw rotation curves between 85 au and an outer radius derived in this paper scaled the stellar distance (400 and 348 pc) in both papers.

These PV diagram helps illustrate two points. First, our choice for the closer distance of 325 au together with a lighter stellar mass is still in agreement with the CO rotation curves. Second, the CO emission is suppressed at the location where the continuum emission is strongest, between 0.34″ and 0.63″. This latter is an artifact of the data reduction, where subtracting the continuum emission suppresses line emission at those locations where the emission is optically thick or, in case of optically thin emission, where the dust in the midplane absorbs some emission coming from the far side of the disk.

We do not detect any kinematical deviation from Keplerian rotation in the CO emission within the gap as predicted for the interaction of Jupiter-mass planets with the gas disk (Perez et al. 2015b). The observations we present are of the highly optically thick ^{12}CO $J = 3-2$ transition and were made with both lower spatial and sensitivity compared to those predictions presented

in Perez et al. (2015b). These three factors all conspire to make a possible kinematical imprint in the gas by the companion more difficult to detect. A deeper observation on an optically thinner isotopologue such as ^{13}CO at ALMA's highest resolution could help uncover a putative companion in HD 34282.

The HCO$^+$ $J = 4-3$ emission is detected in closer proximity to the dust ring starting at the cavity outer radius and extending out to 1.3″. Compared to the CO emission, the HCO$^+$ $J = 4-3$ emission originates closer to the midplane; this is very similar to the emission detected from the HD 97048 disk (van der Plas et al. 2017). Because HCO$^+$ ions quickly disappear without gas-phase CO molecules (e.g. Cleeves et al. 2014), we interpret this height difference as a vertical temperature gradient.

4.4. Comparison of the radial extent of the dust and gas disk

The radial extent of the disk as measured with ^{12}CO $J = 3-2$ emission is a factor of 2.7 larger than the disk measured at 345 GHz. While such a difference can be largely explained by different optical depths for the dust and gas (e.g. Dutrey et al. 1998; Guilloteau & Dutrey 1998) without the need for radial drift of larger particles (Facchini et al. 2017), the sharp drop at 1.15″ is very reminiscent of the drop seen in, for example, the disks around TW Hya (Hogerheijde et al. 2016; Andrews et al. 2016) and HD 97048 (van der Plas et al. 2017). We follow the interpretation in those works that the sharp drop is caused by the outer edge of a drift-dominated dust distribution (Birnstiel & Andrews 2014; Facchini et al. 2017) and the tail end of the radial intensity distribution as a smearing effect by the beam of the outer disk edge at 1.15″.

5. Conclusions

We resolve the disk around HD 34282 in the dust continuum emission at 867 μm into a ring between 0.24 ″ and 1.15 ″ or between 78^{+7}_{-11} and 374^{+33}_{-54} au using a distance of 374^{+33}_{-54}. There is an azimuthal asymmetry present in the dust continuum emission that coincides with the radial position of the ring but is radially unresolved, with an azimuthal extent of 52°, and contains 5% of the total sub-mm flux on top of the background disk emission. We also detect ^{12}CO $J = 3-2$ and HCO$^+$ $J = 4-3$ emission lines. Assuming Keplerian rotation, we detect CO emission between 24 and 1000 au, 2.7 times as far out as the mm dust grains. The sharp outer edge of the dust disk suggests that this is due to radial drift.

We discount photoevaporation as an opening mechanism for the disk cavity. Rather, the disk cavity and azimuthal structure, the presence of gas within the cavity, and the low stellar accretion, all can be explained by the presence of a ≈50 $M_{\rm jup}$ brown dwarf companion in the gap at a distance of ≈0.1″.

Acknowledgements. We thank the referee for the comments which helped to improve the clarity of this paper. This paper makes use of data from ALMA programme 2013.1.00658.S. ALMA is a partnership of ESO (representing its member states), NSF (USA) and NINS (Japan), together with NRC (Canada) and NSC and ASIAA (Taiwan), in cooperation with the Republic of Chile. The Joint ALMA Observatory is operated by ESO, AUI/NRAO and NAOJ. The National Radio Astronomy Observatory is a facility of the National Science Foundation operated under cooperative agreement by Associated Universities, Inc. This work has made use of data from the European Space Agency (ESA) mission *Gaia* (http://www.cosmos.esa.int/gaia), processed by the *Gaia* Data Processing and Analysis Consortium (DPAC, http://www.cosmos.esa.int/web/gaia/dpac/consortium). Funding for the DPAC has been provided by national institutions, in particular the institutions participating in the *Gaia* Multilateral Agreement. G.v.d.P., C.C. and S.C. acknowledge support from the Millennium Science Initiative (Chilean Ministry of Economy) through grant RC130007. G.P. acknowledges financial support from FONDECYT, grant 3140393, L.C. acknowledges support from FONDECYT grant 1171246, and S.C. acknowledges support from FONDECYT grant 1130949. G.P. and F.M. acknowledge funding from ANR of France under contract number ANR-16-CE31-0013 (Planet-Forming-Disks). C.C. acknowledges support from CONICYT PAI/Concurso nacional de insercion en la academia 2015, Folio 79150049. H.A. acknowledges the financial support of the Swiss National Science Foundation within the framework of the National Centre for Competence in Research Planets and H.C. acknowledges support from the Spanish grant AYA 2014-55840-P.

References

Acke, B., Min, M., van den Ancker, M. E., et al. 2009, A&A, 502, L17
Alexander, R. D., Clarke, C. J., & Pringle, J. E. 2006, MNRAS, 369, 216
ALMA Partnership, Brogan, C. L., Pérez, L. M., et al. 2015, ApJ, 808, L3
Amado, P. J., Moya, A., Suárez, J. C., et al. 2004, MNRAS, 352, L11
Andrews, S. M., Rosenfeld, K. A., Kraus, A. L., & Wilner, D. J. 2013, ApJ, 771, 129
Andrews, S. M., Wilner, D. J., Zhu, Z., et al. 2016, ApJ, 820, L40
Artymowicz, P., & Lubow, S. H. 1994, ApJ, 421, 651
Avenhaus, H., Quanz, S. P., Schmid, H. M., et al. 2014, ApJ, 781, 87
Baines, D., Oudmaijer, R. D., Porter, J. M., & Pozzo, M. 2006, MNRAS, 367, 737
Bast, J. E., Brown, J. M., Herczeg, G. J., van Dishoeck, E. F., & Pontoppidan, K. M. 2011, A&A, 527, A119
Birnstiel, T., & Andrews, S. M. 2014, ApJ, 780, 153
Brown, J. M., Blake, G. A., Qi, C., et al. 2009, ApJ, 704, 496
Canovas, H., Schreiber, M. R., Cáceres, C., et al. 2015, ApJ, 805, 21
Canovas, H., Caceres, C., Schreiber, M. R., et al. 2016, MNRAS, 458, L29
Carmona, A., van den Ancker, M. E., Thi, W.-F., Goto, M., & Henning, T. 2005, A&A, 436, 977
Carmona, A., Pinte, C., Thi, W. F., et al. 2014, A&A, 567, A51
Casassus, S., van der Plas, G., M, S. P., et al. 2013, Nature, 493, 191
Casey, M. P., Zwintz, K., Guenther, D. B., et al. 2013, MNRAS, 428, 2596
Clarke, C. J., Gendrin, A., & Sotomayor, M. 2001, MNRAS, 328, 485
Cleeves, L. I., Bergin, E. A., & Adams, F. C. 2014, ApJ, 794, 123
de Gregorio-Monsalvo, I., Ménard, F., Dent, W., et al. 2013, A&A, 557, A133
de Val-Borro, M., Artymowicz, P., D'Angelo, G., & Peplinski, A. 2007, A&A, 471, 1043
Draine, B. T., & Lee, H. M. 1984, ApJ, 285, 89
Dullemond, C. P., & Dominik, C. 2004, A&A, 417, 159
Dutrey, A., Guilloteau, S., Prato, L., et al. 1998, A&A, 338, L63
Dzyurkevich, N., Flock, M., Turner, N. J., Klahr, H., & Henning, T. 2010, A&A, 515, A70
Facchini, S., Birnstiel, T., Bruderer, S., & van Dishoeck, E. F. 2017, A&A, 605, A16
Fairlamb, J. R., Oudmaijer, R. D., Mendigutía, I., Ilee, J. D., & van den Ancker, M. E. 2015, MNRAS, 453, 976
Gaia Collaboration (Prusti, T., et al.) 2016, A&A, 595, A1
Gaia Collaboration (Brown, A. G. A., et al.) 2016, A&A, 595, A2
Garufi, A., Meeus, G., Benisty, M., et al. 2017, A&A, 603, A21
Greaves, J. S., Mannings, V., & Holland, W. S. 2000, Icarus, 143, 155
Gonzalez, J.-F., Laibe, G., & Maddison, S. T. 2017, MNRAS, 467, 1984
Guilloteau, S., & Dutrey, A. 1998, A&A, 339, 467
Hildebrand, R. H. 1983, Quant. J. Roy. Astron. Soc., 24, 267
Högbom, J. A. 1974, A&AS, 15, 417
Hogerheijde, M. R., Bekkers, D., Pinilla, P., et al. 2016, A&A, 586, A99
Honda, M., Maaskant, K., Okamoto, Y. K., et al. 2012, ApJ, 752, 143
Isella, A., Guidi, G. Testi, L., et al. 2016, Phys. Rev. Lett., 117, 25
Kama, M., Folsom, C. P., & Pinilla, P. 2015, A&A, 582, L10
Khalafinejad, S., Maaskant, K. M., Mariñas, N., & Tielens, A. G. G. M. 2016, A&A, 587, A62
Kraus, A. L., & Ireland, M. J. 2012, ApJ, 745, 5
Laibe, G. 2014, MNRAS, 437, 3037
Laor, A., & Draine, B. T. 1993, ApJ, 402, 441
Lovelace, R. V. E., Li, H., Colgate, S. A., & Nelson, A. F. 1999, ApJ, 513, 805
Lyra, W., & Lin, M.-K. 2013, ApJ, 775, 17
Maaskant, K. M., Honda, M., Waters, L. B. F. M., et al. 2013, A&A, 555, A64
Maaskant, K. M., Min, M., Waters, L. B. F. M., & Tielens, A. G. G. M. 2014, A&A, 563, A78
Martí-Vidal, I., Vlemmings, W. H. T., Muller, S., & Casey, S. 2014, A&A, 563, A136
Meeus, G., Waters, L. B. F. M., Bouwman, J., et al. 2001, A&A, 365, 476
Meheut, H., Meliani, Z., Varniere, P., & Benz, W. 2012, A&A, 545, A134
Merín, B., Montesinos, B., Eiroa, C., et al. 2004, A&A, 419, 301

McMullin, J. P., Waters, B., Schiebel, D., Young, W., & Golap, K. 2007, Astronomical Data Analysis Software and Systems XVI, 376, 127
Natta, A., Testi, L., Neri, R., Shepherd, D. S., & Wilner, D. J. 2004, A&A, 416, 179
Nomura, H., Tsukagoshi, T., Kawabe, R., et al. 2016, ApJ, 819, L7
Owen, J. E., Ercolano, B., Clarke, C. J., & Alexander, R. D. 2010, MNRAS, 401, 1415
Pérez, L. M., Carpenter, J. M., Chandler, C. J., et al. 2012, ApJ, 760, L17
Perez, S., Casassus, S., Ménard, F., et al. 2015a, ApJ, 798, 85
Perez, S., Dunhill, A., Casassus, S., et al. 2015b, ApJ, 811, L5
Piétu, V., Dutrey, A., & Kahane, C. 2003, A&A, 398, 565
Pinilla, P., Benisty, M., & Birnstiel, T. 2012, A&A, 545, A81
Pinilla, P., van der Marel, N., Pérez, L. M., et al. 2015, A&A, 584, A16
Pinte, C., Dent, W. R. F., Ménard, F., et al. 2016, ApJ, 816, 25
Pontoppidan, K. M., Blake, G. A., & Smette, A. 2011, ApJ, 733, 84
Ragusa, E., Dipierro, G., Lodato, G., Laibe, G., & Price, D. J. 2017, MNRAS, 464, 1449
Richer, J. S., & Padman, R. 1991, MNRAS, 251, 707
Rosenfeld, K. A., Andrews, S. M., Hughes, A. M., Wilner, D. J., & Qi, C. 2013, ApJ, 774, 16
Rosenfeld, K. A., Chiang, E., & Andrews, S. M. 2014, ApJ, 782, 62
Testi, L., Birnstiel, T., Ricci, L., et al. 2014, Protostars and Planets VI (Tucson: University of Arizona Press), 339
Tsukagoshi, T., Nomura, H., Muto, T., et al. 2016, ApJ, 829, L35
Uribe, A. L., Klahr, H., Flock, M., & Henning, T. 2011, ApJ, 736, 85
van der Marel, N., van Dishoeck, E. F., Bruderer, S., Pérez, L., & Isella, A. 2015, A&A, 579, A106
van der Plas, G., van den Ancker, M. E., Acke, B., et al. 2009, A&A, 500, 1137
van der Plas, G., van den Ancker, M. E., Waters, L. B. F. M., & Dominik, C. 2015, A&A, 574, A75
van der Plas, G., Wright, C. M., Ménard, F., et al. 2017, A&A, 597, A32
van Leeuwen, F. 2007, A&A, 474, 653
Walsh, C., Juhász, A., Pinilla, P., et al. 2014, ApJ, 791, L6
Weidenschilling, S. J. 1977, MNRAS, 180, 57
Weingartner, J. C., & Draine, B. T. 2000, BAAS, 32, 42.07
Wheelwright, H. E., Oudmaijer, R. D., & Goodwin, S. P. 2010, MNRAS, 401, 1199
Williams, J. P., & Cieza, L. A. 2011, ARA&A, 49, 67
Woitke, P., Min, M., Pinte, C., et al. 2016, A&A, 586, A103
Zhang, K., Bergin, E. A., Blake, G. A., et al. 2016, ApJ, 818, L16